ACS NANO

www.acsnano.org

ARTICLE

Revealing Sintering Kinetics of MoS_2-Supported Metal Nanocatalysts in Atmospheric Gas Environments *via Operando* Transmission Electron Microscopy

Boao Song, Timothy T. Yang, Yifei Yuan, Soroosh Sharifi-Asl, Meng Cheng, Wissam A. Saidi,* Yuzi Liu,* and Reza Shahbazian-Yassar*

Cite This: *ACS Nano* 2020, 14, 4074–4086

Read Online

ACCESS | Metrics & More | Article Recommendations | Supporting Information

ABSTRACT: The decoration of two-dimensional (2D) substrates with nanoparticles (NPs) serve as heterostructures for various catalysis applications. Deep understanding of catalyst degradation mechanisms during service conditions is crucial to improve the catalyst durability. Herein, we studied the sintering behavior of Pt and bimetallic Au-core Pt-shell (Au@Pt core–shell) NPs on MoS_2 supports at high temperatures under vacuum, nitrogen (N_2), hydrogen (H_2), and air environments by *in situ* gas-cell transmission electron microscopy (TEM). The key observations are summarized as effect of environment: while particle migration and coalescence (PMC) was the main mechanism that led to Pt and Au@Pt NPs degradation under vacuum, N_2, and H_2 environments, the degradation of MoS_2 substrate was prominent under exposure to air at high temperatures. Pt NPs were less stable in H_2 environment when compared with the Pt NPs under vacuum or N_2, due to Pt–H interactions that weakened the adhesion of Pt on MoS_2. Effect of NP composition: under H_2, the stability of Au@Pt NPs was higher in comparison to Pt NPs. This is because H_2 promotes the alloying of Pt–Au, thus reducing the number of Pt at the surface (reducing H_2 interactions) and increasing Pt atoms in contact with MoS_2. Effect of NP size: The alloying effect promoted by H_2 was more pronounced in small size Au@Pt NPs resulting in their higher sintering resistance in comparison to large size Au@Pt NPs and similar size Pt NPs. The present work provides key insights into the parameters affecting the catalyst degradation mechanisms on 2D supports.

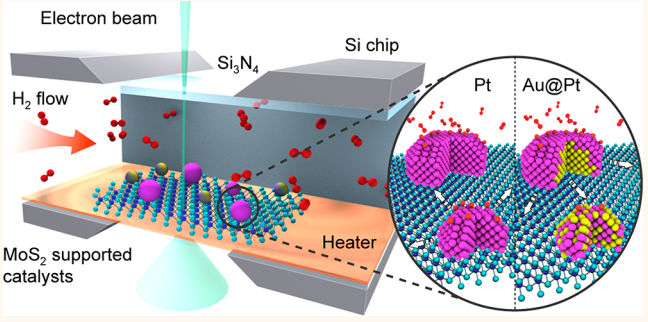

KEYWORDS: *2D materials, in situ TEM, gas-cell, thermal degradation, sintering, noble metal catalyst*

Heterostructures formed from 2D substrate and supported nanoparticles have shown promising applications in catalyst,[1−5] sensor,[6−9] and energy storage fields.[10−12] Among the various 2D supports, MoS_2 is of increasing interest due to its excellent activity for hydrogen evolution reaction (HER)[13] and chemical sensing.[9] Specifically, the heterostructures of MoS_2 supported nanosize metal nanoparticles display better HER activity than commercial Pt/C catalyst, such as Pt–MoS_2,[14,15] Rh–MoS_2 composite,[16] Co-doped MoS_2,[17] and Ni_2P–MoS_2,[18] with additional benefit of reducing expensive Pt loading in a catalytic system.

A major challenge in catalysts is the degradation of catalyst nanostructures due to irreversible sintering during service conditions that involve exposure to various gases at elevated temperatures.[19] Such catalyst nanostructure coarsening usually results in loss of active surface area and intended catalytic properties. It is therefore crucial to develop reliable methods to control catalyst size and shape and prevent sintering, especially in working environments. There are various examples: Pt decorated Co–Pd core–shell catalysts are shown to have high stability and better oxygen reduction reaction (ORR) activity than commercial Pt catalysts;[20] atomically dispersed dinuclear Ir catalysts anchored on α-Fe_2O_3 has been reported with good

Received: November 5, 2019
Accepted: April 13, 2020
Published: April 13, 2020

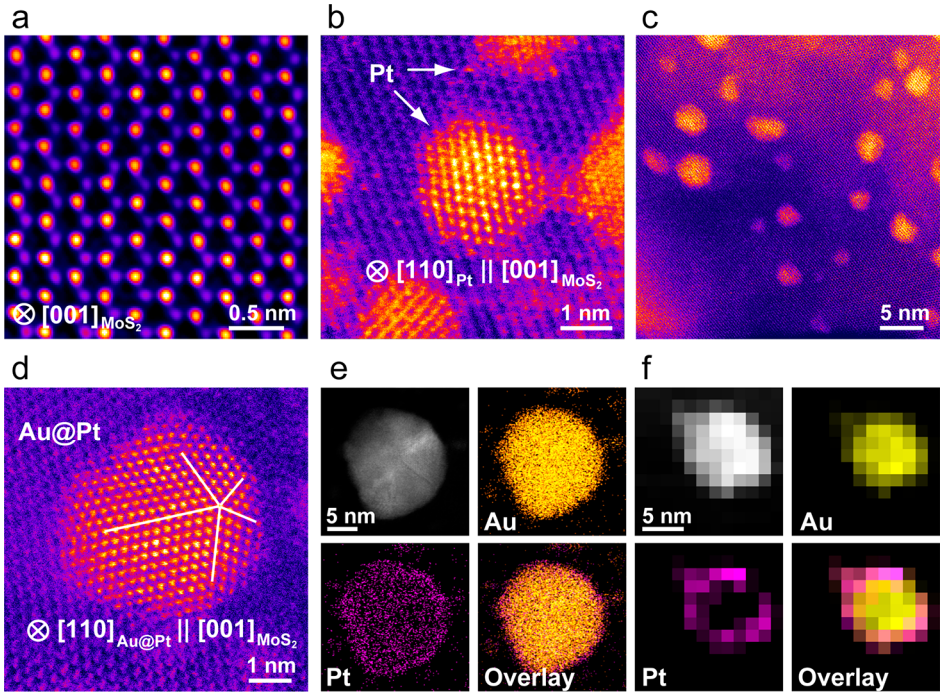

Figure 1. Atomic structure and chemical characterization of Pt and Au@Pt core−shell NPs on MoS_2 support. False-color atomic HAADF images showing (a) MoS_2 (b) Pt, and (c, d) Au@Pt core−shell NPs on MoS_2 support. The EDS (e) and EELS (f) mappings of Au, Pt, and the overlaid map. The yellow and magenta colors correspond to Au and Pt, respectively.

stability against detachment and aggregation;[21] Au−Pt core−shell star-shaped decahedra displays high stability in ORR environments.[22] Further attention is paid on design of substrates to enhance metal−support interactions and inhibit catalyst particle migration,[23] such as spinel $MgAl_2O_4$ for Pt support,[24] porous carbon for Pt and $PtCo_x$,[25] and very recently 2D supports including graphene[26] and MoS_2.[27] However, an in-depth understanding of anchor effects and degradation mechanisms for 2D substrates supported heterogeneous catalysts is still lacking.

Recently, various *in situ* experimental techniques are under fast development such as *in situ* X-ray scattering,[28,29] *in situ* X-ray photoelectron spectroscopy (XPS),[30,31] and *in situ* TEM[26,32−42] to overcome the barrier of revealing catalyst dynamics. Among them, advances in the field of *in situ* environmental transmission electron microscopy (ETEM) provide opportunity to obtain both atomic structural and chemical composition information on particle evolution during catalytic reactions. To perform such ETEM studies, either the microscope column can be modified to enable the exposure of specimens to gas environment[43−49] or the specimen holder can be designed to accommodate the microfabricated gas-cell devices.[36,50−60] The latter setup provides the possibility to observe samples in gases at atmospheric pressure with little resolution degradation, allowing the real time analysis of materials in *operando* conditions. For instance, the CO oxidation reaction on Pt/C was investigated and Pt nanoparticle surface reconstruction was captured in real time.[59] In another work, the transformation of PdCu nanocatalyst from spherical to truncated cubes was observed in H_2 environment.[60] Very recently, formation of NiO shell over Pt−Ni bimetallic nanocatalysts during oxidation and reduction reactions were reported and an enhanced catalytic activity was found in a Pt−NiO format.[61]

Despite the extensive research on catalyst evolution in gases environment, how 2D supported catalysts behave in gas and high temperature conditions is not well understood. For example, it is unclear whether a 2D heterostructure catalyst system can maintain good thermal stability against sintering especially during high temperature electrolysis operations that involves H_2 gas.[62] Here, we report an *in situ* environmental gas-cell TEM study of sintering behavior of Pt and Au@Pt core−shell NPs on 2D MoS_2 support from room temperature (rt) to 400 °C in vacuum and N_2, H_2, and air at atmospheric pressure. MoS_2 support exhibits sufficient stability during heating in vacuum, N_2, and H_2, while degradation of MoS_2 is observed when heating in air. We found that sintering of Pt and Au@Pt on MoS_2 in vacuum, N_2, and H_2 was mainly governed by the PMC mechanism. More importantly, H_2 plays a vital role in controlling the degradation mechanism. High-resolution TEM (HRTEM) results reveal stronger diffusion and rotation of Pt NPs during coalescence in H_2 than in vacuum environment. This is due to the Pt−H interactions that weaken the adhesion of Pt NPs on MoS_2. In contrast, Au@Pt NPs display better stability than Pt in H_2, especially for the smaller size Au@Pt NPs. This is attributed to H_2 adsorption promotes the alloying effect on smaller Au@Pt NPs and results in reduced Pt−H interaction and increase of Pt in contact with MoS_2 that lead to better sintering resistance at elevated temperatures.

RESULTS AND DISCUSSION

Before *in situ* experiments, the morphology of synthesized Pt and Au@Pt core−shell NPs on MoS_2 were characterized by atomic resolution scanning transmission electron microscopy (STEM). Figure 1a shows false-color high-angle annular dark-field (HAADF) image of pristine MoS_2 nanoflake before metal NPs deposition. The nanoflake is in 2H phase on ⟨001⟩ zone axis with (001) basal plane perpendicular to electron beam. HAADF image in Figure 1b shows the Pt NPs grown on MoS_2

https://dx.doi.org/10.1021/acsnano.9b08757
ACS Nano 2020, 14, 4074−4086

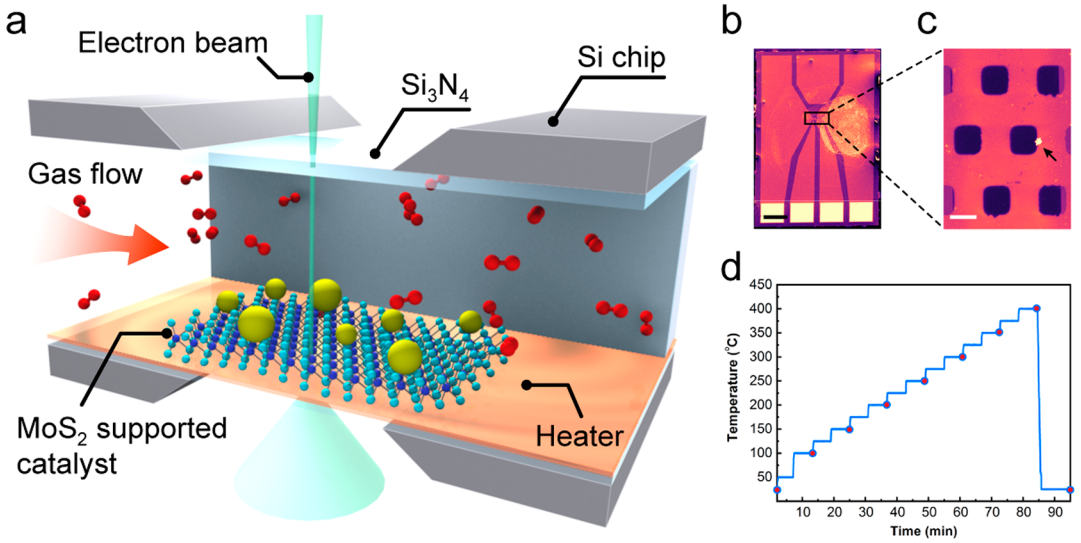

Figure 2. ***In situ*** **gas-cell TEM system, microfabricated gas-cell devices and temperature profile. (a) Schematic of** ***in situ*** **gas-cell TEM to study catalytic reactions. (b) SEM image of the microchip with drop-casted sample on it. Scale bar is 0.5 mm. (c) Higher magnification SEM image focusing on the Si_3N_4 window area in b. The heater area is shown as brighter contrast region. Arrow points to a representative MoS_2 nanoflake with NPs on it. Scale bar is 5 μm. (d) Temperature profile for each** ***in situ*** **experiment. Red dots represent the time at which image was acquired (more information in the Methods).**

support, with epitaxial relationship of $(110)_{Pt}$ parallel to $(001)_{MoS2}$ basal plane. Figure 1c shows a lower magnification HAADF image including several Au@Pt NPs. Atomic resolution Au@Pt core−shell NP is shown in Figure 1d with 5-fold twining on ⟨110⟩ zone axis, suggesting the same epitaxial relationship as Pt. Since the Z (atomic number) contrast difference between Au and Pt in HAADF image is not obvious to differentiate, energy-dispersive X-ray spectroscopy (EDS) and electron energy-loss spectroscopy (EELS) were performed to further determine the elemental distribution. Different from EDS mapping for pristine Pt (Figure S1a), mapping for Au@Pt shown in Figure 1e indicates an Au core and Pt outer layer. The EDS line scan profile in Figure S1b,c shows another example of an Au@Pt NP. Similar to EDS, EELS mapping in Figure 1f suggests a core−shell structure for Au@Pt by extracting Au and Pt $M_{4,5}$ edges from the core-loss region. Detailed EELS maps including Mo $L_{2,3}$ and S K edge as well as spectra collected at Au core and Pt shell regions are included in Figure S2.

For *in situ* environmental gas-cell TEM experiments, a schematic illustration of specimen holder is shown in Figure 2a. The isolated environment formed by a pair of microchips allows continuous gas flow at atmospheric pressure inside the cell.[36,50,51] The obtained Pt and Au@Pt NPs on MoS_2 were loaded onto one microchip with a heater layer, as shown in scanning electron microscopy (SEM) image in Figure 2b. A representative MoS_2 nanoflake is marked by an arrow in higher magnification SEM image (Figure 2c). The temperature profile for each *in situ* experiment is shown in Figure 2d, with red dots representing the time when images were acquired. It is worth noting that resolution degradation due to window bulging effect for gas-cell TEM is much less than liquid-cell TEM since gases usually have density 3 orders of magnitude lower than general solutions used for liquid-cell TEM.[51] However, samples located close to the corner and edge of Si_3N_4 window are preferentially selected for imaging to reduce multiple electron scattering and thus ensure a maximized imaging resolution.

Effect of Environment on Nanoparticle Degradation. The *in situ* TEM experiments were performed to investigate the effect of environment on nanoparticle-decorated 2D substrates. First, the sintering behavior of Pt in vacuum during heating to 400 °C was investigated and shown in the TEM image sequences as Figure 3a. Regions marked with rectangle box highlight exemplar areas where particle sintering happens. The coalescence of some Pt NPs can be seen gradually as the temperature rises to 400 °C. When the environment changed to H_2 as shown in Figure 3b, the coalescence of Pt NPs was more obvious compared to heating in vacuum.

Next, for Au@Pt NPs on MoS_2, Figure 3c depicts the morphological evolution during heating in vacuum. Coalescence is seen to happen clearly at exemplar regions marked with boxes. When heating occurred in H_2 environment (Figure 3d), in contrast, less evidence of coalescence of Au@Pt NPs was observed. The statistical variation of nanoparticle coalescence in different evaluated system is explained below.

TEM images were collected from repeated experiments to extract statistical information regarding to particle size distribution (PSD), shown as violin plots for Pt in vacuum and H_2 (Figure 3e,f) and Au@Pt in vacuum and H_2 (Figure 3g,h) at temperatures of rt, 100, 200, 300, and 400 °C. The hollow circle indicates the mean particle size in each distribution. In these violin plots, the vertical distribution shows the size range of nanoparticle, while the horizontal distribution indicates the frequency (or density) of the observed nanoparticles at any particular size.

Both Pt and Au@Pt NPs have narrowed size distribution with a mean particle size of around 4 nm at rt. For Pt NPs heating in vacuum (Figure 3e), as temperature increases broadening and a more log-normal-like PSD can be observed accompanied by the increase of mean particle size. It is known that particle sintering is mainly guided by two mechanisms: PMC and Ostwald ripening.[63] It has been reported that the enlargement of extended long tail in larger particle size region serves as direct evidence that sintering process is guided more through PMC than Ostwald ripening,[25,64] which is similar as

https://dx.doi.org/10.1021/acsnano.9b08757
ACS Nano 2020, 14, 4074−4086

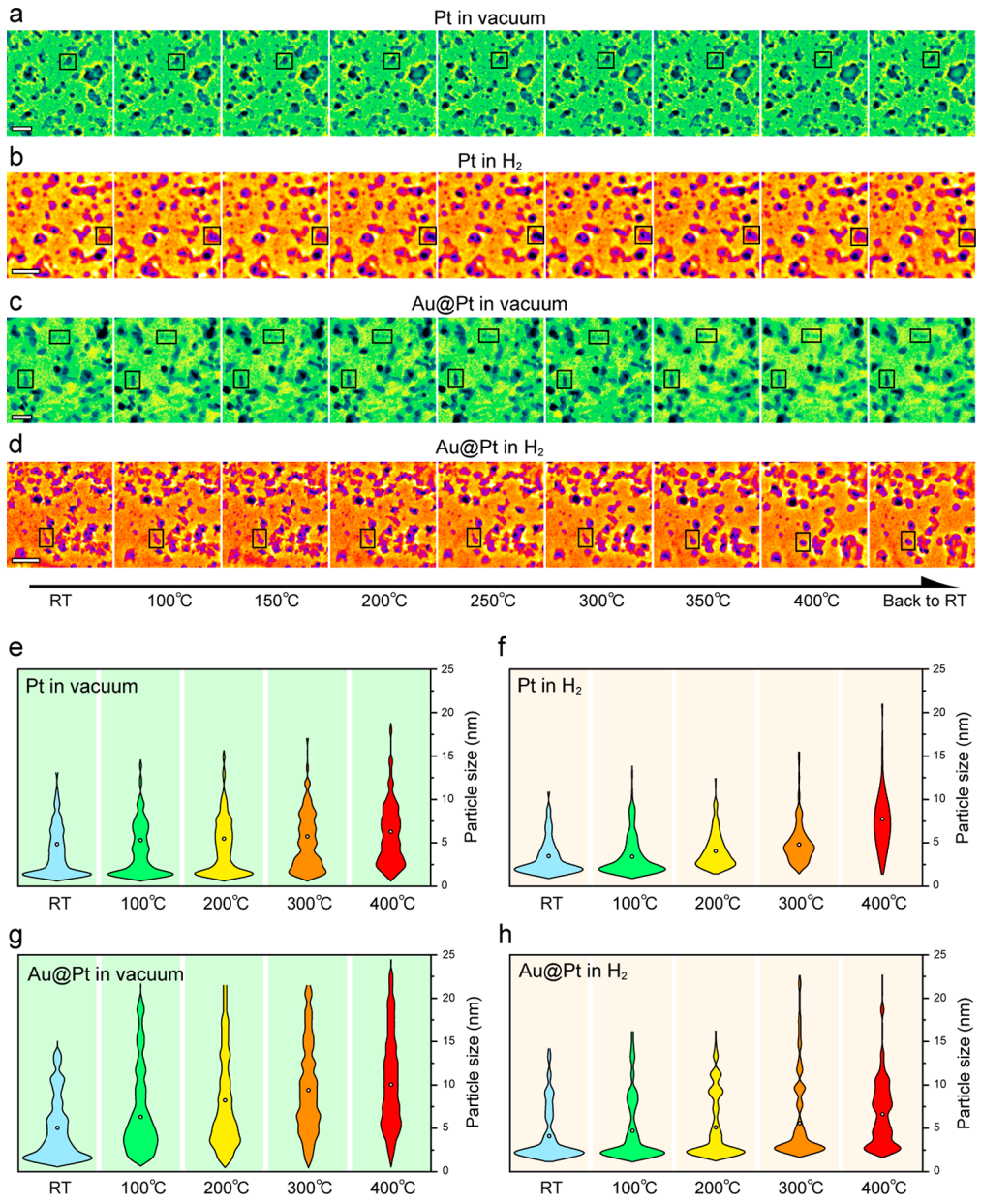

Figure 3. Morphological and statistical analysis of Pt and Au@Pt NPs on MoS_2 during heating from rt to 400 °C in vacuum and H_2. (a, b) TEM image sequences of Pt on MoS_2 during heating to 400 °C in vacuum and H_2. (c, d) TEM image sequences of Au@Pt on MoS_2 during heating to 400 °C in vacuum and H_2. Scale bar is 20 nm for all images. (e, f) Violin plots of particle size distribution of Pt NPs during heating in vacuum and H_2. (g, h) Violin plots of particle size distribution of Au@Pt NPs during heating in vacuum and H_2. Hollow circles mark the mean particle size in each distribution.

what are shown here for Pt NPs heating in vacuum (Figure 3e). For Pt NPs heated in H_2 (Figure 3f), the PSD has more extended log-normal-like tail and larger mean particle size than in vacuum, suggesting the same PMC mechanism but more significant sintering.

For Au@Pt NPs in vacuum (Figure 3g), the broadening of PSD and extended tail indicate the PMC mechanism leading to sintering process. In contrast, Au@Pt NPs in H_2 (Figure 3h) show a much lower broadening of PSD and smaller extended tail compared to vacuum, suggesting much less sintering.

One should note that the MoS_2 substrate did not show evidence of degradation when exposed to temperatures up to 400 °C in vacuum, N_2, and H_2 environments. Figure S3 shows the selected area electron diffraction (SAED) patterns for Pt (Figure S3a) and Au@Pt (Figure S3b) on MoS_2 collected at rt and after heating and cooling to rt in H_2, respectively. Diffraction spots from $\{100\}_{MoS2}$ (marked with hexagonal lines) and $\{110\}_{MoS2}$ remain unchanged in both experiments suggesting a stable MoS_2 under H_2 environment. No significant difference occurred between diffraction rings from {111}, {200}, and {220} before and after heating for both Pt and Au@Pt (marked with half circles). *In situ* heating in air flow containing 21 vol % O_2 was also investigated, but severe structural degradation of MoS_2 support was observed, as shown in TEM and SAED patterns in Figure S4. The reaction between O plasma/O_2 molecule and MoS_2 may explain the structural degradation of MoS_2.[65] Therefore, air flow experiments were not involved in comparison of NP sintering behaviors due to support degradation.

https://dx.doi.org/10.1021/acsnano.9b08757
ACS Nano 2020, 14, 4074−4086

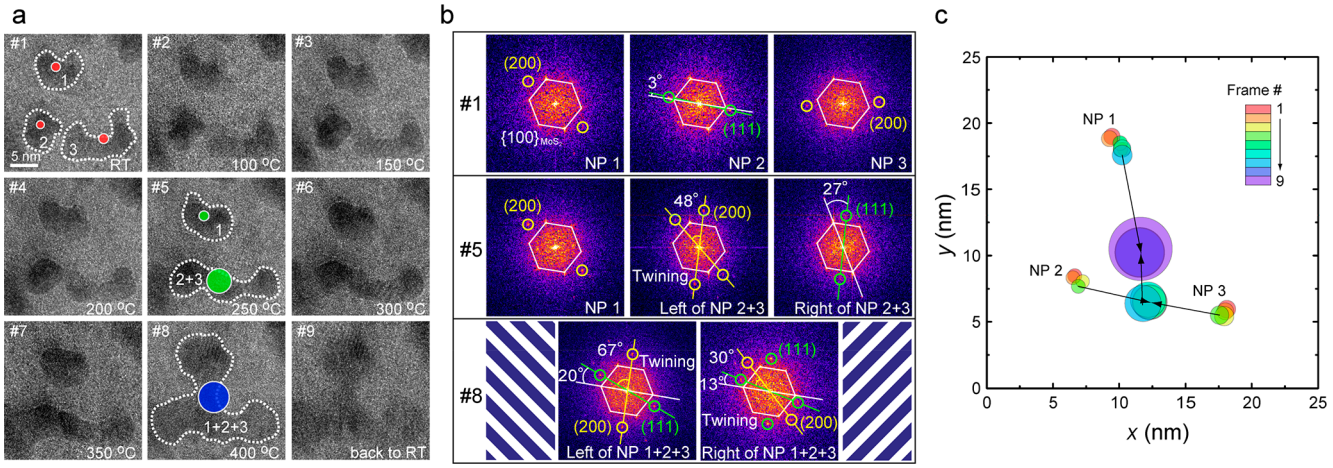

Figure 4. HRTEM of Pt NPs crystallinity evolution during sintering. (a) HRTEM image sequences of Pt NPs sintering on MoS_2 under H_2 from rt to 400 °C. Three NPs are identified with dashed outlines and marked as 1, 2, and 3. (b) FFT of Pt NPs 1, 2, and 3 in frames #1, #5, and #8 in a. Diffraction spots from $\{100\}_{MoS2}$, $(111)_{Pt}$, and $(200)_{Pt}$ are shown in white, green and yellow, respectively. (c) Center of mass evolution of the Pt NPs corresponding to a. Arrows indicate the coalescence process.

Effect of Composition on Nanoparticle Degradation. Here, the comparison is focused on the differences between Pt and core−shell Au@Pt NPs behavior under the same environment. For heating in vacuum, the PSD of Au@Pt NPs (Figure 3g) broadening and formation of an extended long tail happens at relatively lower temperature compare to Pt (Figure 3e), suggesting a more obvious sintering process. In contrast, in H_2 environment the Au@Pt NPs (Figure 3h) display slightly more sintering resistance than Pt (Figure 3f) as the smaller mean particle size.

To further understand such effect of composition, HRTEM imaging was performed *in situ* at each temperature focusing on individual NPs. For heating in vacuum, Pt and Au@Pt are shown in parts a and b, respectively, of Figure S5a and b. Evidence of diffusion of Pt NPs (Figure S5a) can be seen from the shape change of NP #2 and decrease of its distance to NP #1, but without obvious coalescence. This is consistent with the PSD profile that Pt sintering in vacuum is less significant compared to that in H_2. Au@Pt NPs (Figure S5b), however, diffuse and coalesce at relatively lower temperature (less than 200 °C) and both small and large NPs have a tendency to diffuse on MoS_2 support, as indicated by five NPs numbered 2, 3, 4, 5, and 6 coalesced into one from rt to 200 °C. There is not much further morphological change at higher temperatures. These observations are again consistent with the Au@Pt PSD profile containing an extended long tail of larger NPs that indicate PMC. In addition, the heating experiments under N_2 flow and HRTEMs in Figure S6 indicate similar sintering behaviors for both Pt and Au@Pt NPs as under vacuum conditions (details in Supporting Note S1). Thus, these results suggest that N_2 gas does not show significant effect altering the degradation mechanism.

For the case of heating in H_2 environment, the example of Pt NPs sintering under H_2 (Figure 4) clearly depicts the PMC process. In the HRTEM image series (Figure 4a) the orientation of three similarly sized Pt NPs can be resolved (identified as 1, 2, and 3). Particle 2 undergoes partial coalescence with particle 3 at 250 °C, followed by second coalescence with particle 1 at 400 °C, as indicated by the outlines in frames #1, 5, and 8. The dot on each particle represents the location of the center of mass and its diameter is proportional to the particle size. Figure 4b shows the fast Fourier transform (FFT) patterns at region of particles 1, 2, and 3 in frames #1, 5, and 8. The white hexagons indicate diffraction spots from six $\langle 100\rangle_{MoS2}$ directions and also confirms that $(001)_{MoS2}$ basal plane is perpendicular to the viewing direction. These unchanged $\{001\}_{MoS2}$ patterns again suggest the support is stable in the selected temperature range. In each FFT, diffraction spots from $(111)_{Pt}$ and $(200)_{Pt}$ are highlighted by green and yellow circles to analyze the orientation relation with MoS_2 basal plane. It was found that the migration of Pt NPs also involves particle rotation evidenced through the change of $[111]_{Pt}$ and $[200]_{Pt}$ directions. For instance, the [200] direction of particle 1 remains unchanged from rt (frame #1) to 250 °C (frame #5), while at 400 °C (frame #8) this (200) plane disappeared after coalescence with particle 2 and 3, accompanied by formation of new (111) planes. Similarly, particles 2 and 3 both undergo complex rotations and reconstructions involving the change of [111] and [200] directions during coalescence. It is interesting to note that the misalignment angle between $[111]_{Pt}$ and one $[100]_{MoS2}$ direction can change dramatically during particle coalescence, marked as 3°, 27°, 20°, 13° for particle 2 at rt (frame #1), the right portion of particle 2 and 3 at 250 °C (frame #5), and the left and right portion of particles 1, 2, and 3 at 400 °C after coalescence (frame #8). In addition, the irregular angles between certain [111] and [200] directions indicate the formation of twining in all coalesced Pt particles. The PMC processes are further shown in Figure 4c by the center of mass evolution of each particle, with the spot diameter proportional to particle size. In comparison with sintering behavior of Pt NPs in vacuum environment, H_2 is promoting the diffusion and coalescence by increasing the NPs migration distance. Again, these observations are consistent with the PSD profile containing an extended long tail of larger NPs that indicates PMC. Although direct evidence of Ostwald ripening that Pt adatom migrating from small particle toward large particle is beyond observation capability, it is still more plausible that the Pt sintering under atmospheric pressure H_2 is guided by PMC because (1) Ostwald ripening usually involves both particle growth and shrinking and (2) does not induce obvious migration.[45] The slight size increase of each Pt before coalescence suggests Ostwald ripening may also happen by sacrificing tiny NPs but is less significant.

https://dx.doi.org/10.1021/acsnano.9b08757
ACS Nano 2020, 14, 4074−4086

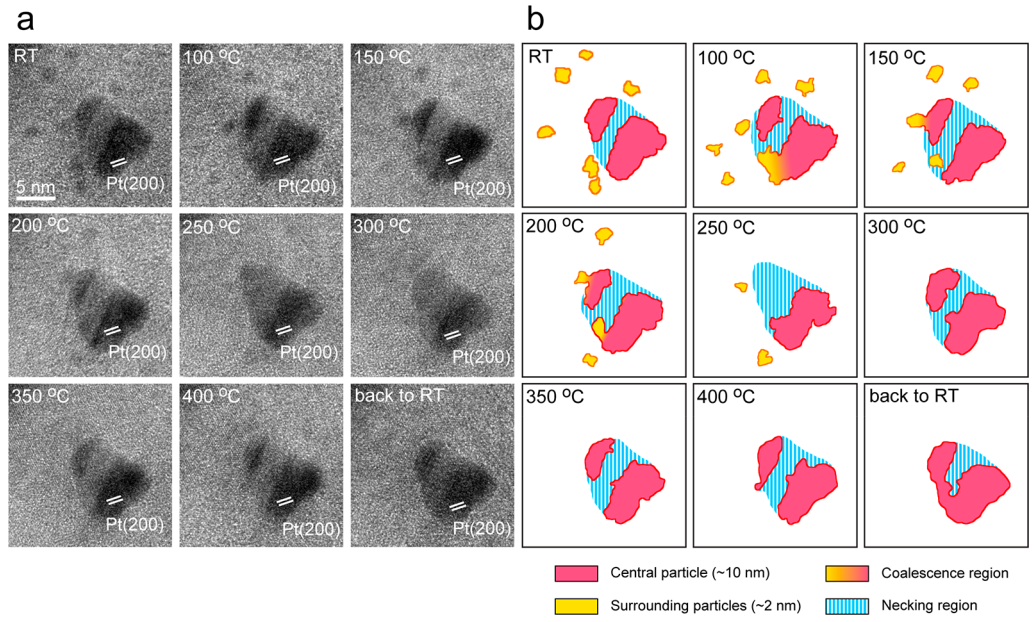

Figure 5. HRTEM of Pt NPs sintering with different sizes. (a) HRTEM image sequences of Pt NPs on MoS_2 under H_2 from rt to 400 °C. (b) Outline of the projected area of Pt NPs corresponding to a.

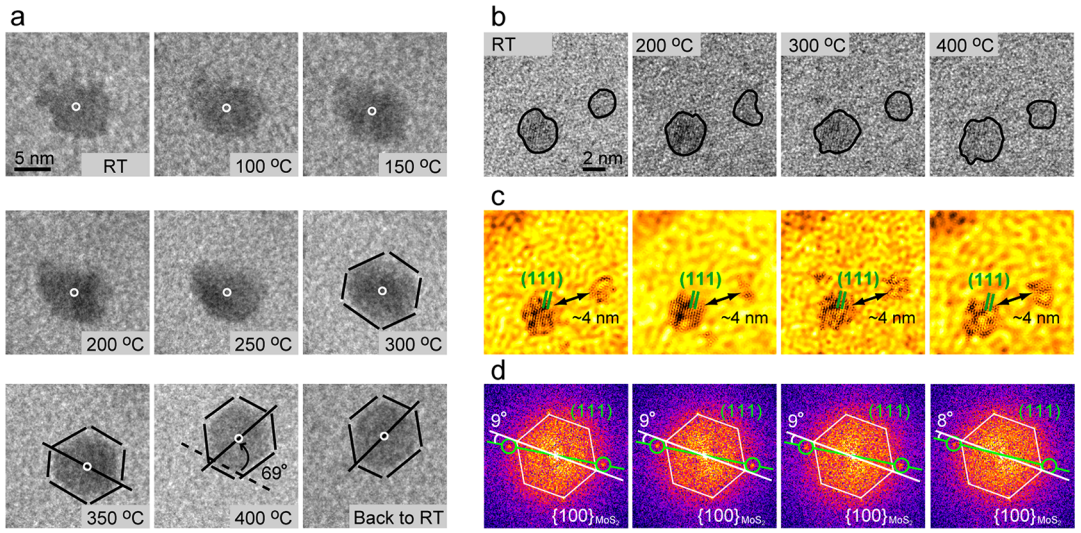

Figure 6. TEM and HRTEM analysis of Au@Pt NPs on MoS_2 during heating in H_2. (a) TEM image sequence of a 10 nm Au@Pt NP on MoS_2 in H_2. Black lines outline the NP boundary and hollow circles mark the location of center of mass. (b) HRTEM image sequence of several smaller Au@Pt NPs (≤5 nm) on MoS_2 in H_2. Two exemplar Au@Pt NPs are outlined with black lines. (c) Filtered images corresponding to b. $(111)_{Au@Pt}$ is marked in green and distance between two NPs marked with arrows. (d) FFT of TEM image sequence in b. Diffraction spots from $\{100\}_{MoS2}$ and $(111)_{Au@Pt}$ are shown in white and green.

For the sintering behavior of Au@Pt in H_2, it is important to take the size effect into consideration when compare to Pt NPs in H_2. Therefore, the discussion will be fully expanded in the subsequent section.

Effect of Particle Size on Nanoparticle Degradation. In Figure 3f, the PSD of Pt NPs in H_2 indicates a gradual loss of smaller Pt NPs at higher temperature. However, it is interesting to note that the PSD for Au@Pt in H_2 (Figure 3h) shows a heavier density of small particle (<5 nm) even at 400 °C, resulting in a less symmetric distribution compare to other conditions. This indicates the less loss of smaller Au@Pt NPs in H_2 environment.

To fully understand the particle size effect, HRTEM was performed *in situ* on smaller and larger NPs for both Pt and Au@Pt. For the case of Pt heating in H_2, Figure 5a shows the evolution of a larger (>10 nm) Pt NP in the center and several surrounding smaller (<5 nm) NPs during heating. At rt, six particles with ∼2 nm in diameter are clearly distinguishable around the central Pt particle. As the temperature rises, these smaller particles gradually diffuse closer to the central one and merge together. At temperatures above 300 °C, all of the smaller particles have disappeared. By masking the spots from FFT for each HRTEM (Figure S7), the outline of particles (Figure 5b) corresponding to each frame in Figure 5a better illustrates the sintering process that involves migration of smaller particles toward central larger particle as well as coalescence when they come in contact. The Pt (200) plane in the central particle is identifiable and can be used to determine

https://dx.doi.org/10.1021/acsnano.9b08757
ACS Nano 2020, 14, 4074−4086

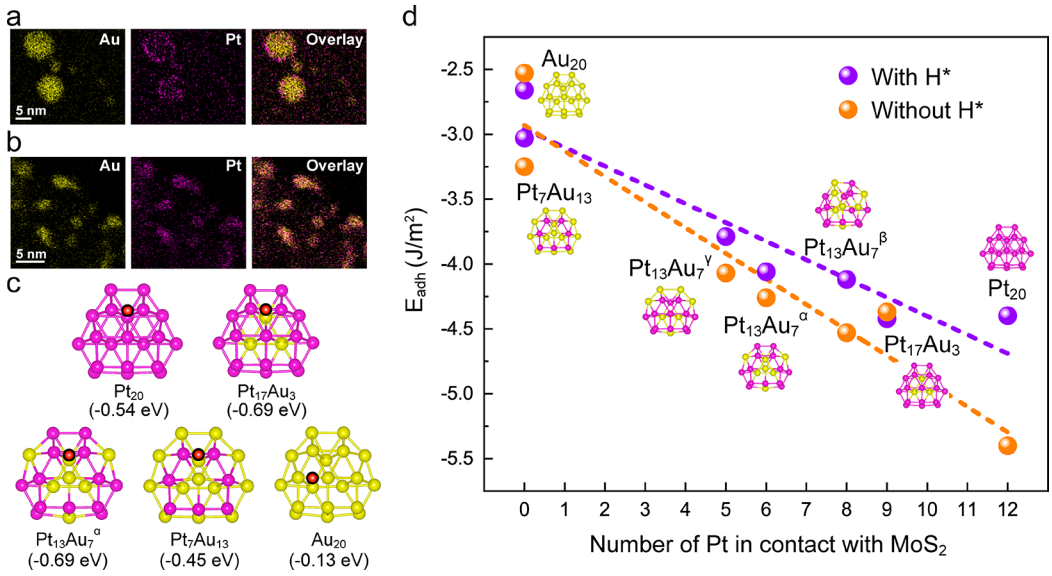

Figure 7. (a, b) *Post situ* EDS analysis on Au@Pt NPs after heating in H_2 in large and small sizes, respectively. (c) MoS_2 supported 20-atom NPs models with different Au/Pt ratios. The strongest H adsorption sites for each structure are indicated by red dots. The ΔG_H of the adsorption sites are listed in parentheses. (d) Adhesion energies of the NPs as a function of number of Pt in contact with MoS_2 support. The trends are shown as purple and orange lines for the NPs with and without H*, respectively.

crystal domains (pink regions). Contrast between two (200) domains (blue stripes) suggests the necking region. During the coalescence of smaller particles, (200) domains in the central particle slightly enlarged but maintained a fixed direction, suggesting it is relatively more stable than the smaller surrounding Pt particles. These results suggest that smaller Pt NPs are less stable than larger Pt NPs in H_2.

For Au@Pt core−shell NPs in H_2, the sintering behavior is presented in Figure 6. The TEM image series in Figure 6a shows a relatively larger Au@Pt in 10 nm size during heating, with the center of mass marked by hollow circles. From rt to 300 °C there is slight surface reconstruction induced particle shape change, but the migration of the NP is not apparent. When the temperature is above 300 °C, migration becomes obvious with a clearer change in the center-of-mass location. The particle became faceted with formation of more distinct corner and edges outlined in the last four frames. By comparing one of the diagonals, a 69° rotation from 350 to 400 °C can be observed, suggesting the migration is accompanied by particle rotation as well. Similar to Pt on MoS_2, such dynamics happen on Au@Pt NPs could be the main reason for particle coalescence and size increase. However, in contrast to larger Au@Pt, the smaller size Au@Pt NPs behave differently as shown in HRTEM image series in Figure 6b. The two outlined particles in size of ∼3 nm display no obvious migration from rt to 400 °C. Filtered HRTEM images in Figure 6c give a clearer view of the lattice of $(111)_{Au@Pt}$ in the larger particle, and the distance between two particles remains 4 nm, indicating the absence of both rotation and migration. FFTs corresponding to Figure 6b shown in Figure 6d indicate that there is no change in the misalignment angle between $[111]_{Au@Pt}$ and one of the $[100]_{MoS2}$ direction, again confirming that such small Au@Pt NP has no rotation during the whole heating process. This significantly diminished diffusion and coalescence of small size Au@Pt NPs is consistent with the PSD that heavier density of smaller particles is present at higher temperatures. In addition, the smaller size Au@Pt display even better stability compare to similar size Pt NPs, again consistent with the PSD profile in Figure 3.

To fully understand the particle size effect, analytical EDS and EELS characterization on *post situ* Au@Pt samples was carried out on smaller and larger Au@Pt NPs on MoS_2. Figure S8 shows EELS mappings of Au@Pt NPs after heating in vacuum. It can be seen that both smaller (Figure S8a) and larger (Figure S8b) NPs maintain the core−shell structure after heating, suggesting no significant NPs structural change when there is no H_2 gas. In sharp contrast, EDS mappings in Figure 7a-b and EELS mappings in Figure S9 show that larger NPs maintained roughly core−shell structure after heating in H_2, while these mappings do not seem to reveal a clear core−shell structure for smaller Au@Pt NPs (mostly less than 5 nm). Therefore, it is suggested that these smaller Au@Pt NPs underwent a core−shell to alloy transformation. Based on DFT calculations, the processes of swapping Pt and Au atoms close to the edges of NPs are feasible with low energy barriers of ∼0.2 eV (Figure S10). The observation suggests that smaller Au@Pt NPs are more likely to be alloyed than larger ones in H_2 at elevated temperatures due to shorter diffusion distance of surface Pt toward the core and bottom Au toward the interior of NPs, and H_2 is essentially playing a vital role in promoting the small NPs alloy formation.

To aid in the understanding of the effect of H_2, composition, and size in sintering behaviors of Pt and Au@Pt core−shell NPs on MoS_2, DFT calculations were performed to analyze H_2 dissociation, $H_2 \rightarrow H^* + H^*$, on Pt, Au and Au@Pt NPs surfaces and their effects on NPs stability. The thermodynamic accessibility of H_2 dissociation is studied using the hydrogen chemisorption Gibbs free energy ΔG_H defined as

$$\Delta G_H = \Delta E_{ads} + \Delta E_{ZPE} - T\Delta S \quad (1)$$

with

$$\Delta E_{ads} = E_{NP/MoS_2/nH} - E_{NP/MoS_2} - 0.5nE_{H_2(g)}$$

where $E_{NP/MoS_2/H}$ and E_{NP/MoS_2} are, respectively, the total energies of a system with n adsorbed hydrogen atom(s) H*

https://dx.doi.org/10.1021/acsnano.9b08757
ACS Nano 2020, 14, 4074−4086

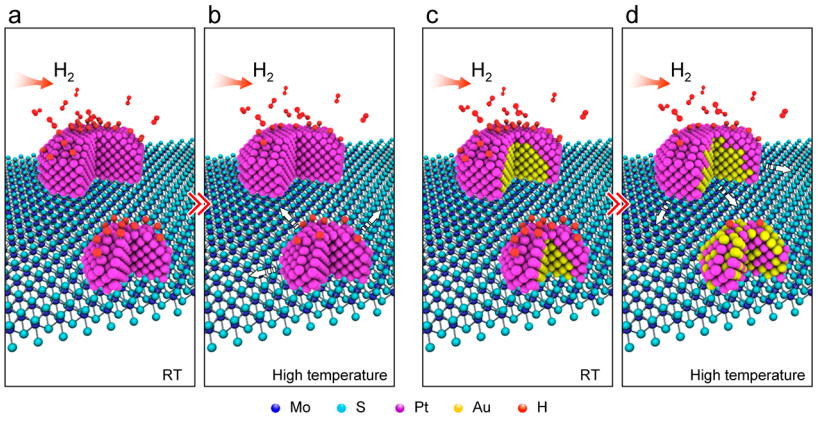

Figure 8. Schematic illustration of (a, b) Pt and (c, d) Au@Pt core−shell NPs behavior on MoS_2 at rt and higher temperature up to 400 °C in H_2 environment.

and with no H*. $E_{H_2}(g)$ is the energy of H_2 molecule in vacuum. The difference in zero-point energy ΔE_{ZPE} between H* and $H_2(g)$ is approximated to 0.04 eV, which is the value obtained on metal surfaces.[66] At T = 298 K, experimental results were used to estimate the entropic contribution $T\Delta S$ = −0.2 eV.[66] With a positive ΔG_H, hydrogen in gas phase is more stable than in adsorbed state and *vice versa* for a negative ΔG_H. Next, models of MoS_2 supporting 20-atom NPs were employed to study the single hydrogen atom adsorption events on alloys Au_iPt_j at different atomic ratios of i and j as well as pure Au_{20} and Pt_{20} NPs, as shown in Figure 7c. Note that $Pt_{13}Au_7$ is investigated under three different configurations as shown in Figure S11, named α, β, and γ. The strongest H adsorption site is at the bridge sites between two metal atoms. Comparing these systems, ΔG_H is the most negative for $Pt_{17}Au_3$ and $Pt_{13}Au_7{}^{\alpha}$ followed by Pt_7Au_{13} and Pt_{20} and is the least negative for Au_{20}. Such information implies that the hydrogen dissociation is the most thermodynamically favorable on $Pt_{17}Au_3$ and $Pt_{13}Au_7{}^{\alpha}$ and the least for Au_{20}. In addition, the reaction pathways of hydrogen dissociation (Figure S12) on Pt_{20} and $Pt_{13}Au_7{}^{\alpha}$NPs are barrierless, which is in accordance with the low ΔG_H of −0.54 and −0.69 eV, respectively. In contrast, a relatively high barrier of 0.42 eV is observed on Au_{20} NP with ΔG_H = −0.13 eV. The density of states (DOS) of the NPs, as shown in Figure S13, explain the hydrogen adsorption events. For Au_{20} with the metallic d-band located far below the Fermi level ($E - E_F = 0$), as indicated by the peak of d-band (E_p), its interaction with H* is relatively weak compare to Pt_{20} and the alloyed NPs with the d-band located close to the Fermi level. This is explained by the d-band theory; upon hydrogen adsorption, the d-band splits into bonding and antibonding states located below or above E_p, respectively, and the filling of the antibonding states make the system less stable. For Au_{20} that has a lower E_p, its antibonding states are located more closer to E_F thus are more easily to be occupied comparing to Pt_{20} and alloyed NPs which have higher E_p. This suggests that Au is more inert to H_2 dissociation compared to Pt and Au@Pt NPs and therefore provides the evidence that the stabilities of Pt and Au@Pt in hydrogen ambient can be affected by structural change induced by hydrogen adsorption. To show this more, the stabilities of the NPs on MoS_2 support are gauged from the adhesion energy defined as[67,68]

$$E_{adh} = (E_{NP/MoS_2} - E_{NP} - E_{MoS_2})/A \quad (2)$$

where E_{NP/MoS_2}, E_{NP}, and E_{MoS_2} are the DFT energies of the MoS_2-supported NP, nonsupported NP and MoS_2, respectively, A is the contact surface area between MoS_2 and NPs. The impact of hydrogen adsorption on E_{adh} can also be determined using eq 2 where E_{NP/MoS_2} and E_{NP} represent the DFT energies of the MoS_2 supported and nonsupported NPs with H*. The hydrogen adsorption configurations are obtained by occupying the strong adsorption sites evaluated by single-hydrogen adsorption events, as we have previously shown that H* − H* repulsions have minimal effects on the hydrogen configurations for surfaces with strong hydrogen interaction.[69] Figure 7d, and the values in Table S1 show the decreasing trend of E_{adh} with the increasing number of Pt in contact with MoS_2 surface for the NPs with and without H*. It can be concluded that H* decreases NPs stabilities for most of structures. Furthermore, the temperature effect on NPs' stability is also analyzed by calculating temperature-dependent adhesion energies $E_{adh}(T)$ with and without H*. The overall results show that temperature effect is relatively small (details are provided in Supporting Note S2 and Figure S14).

Combining all of the experimental and theoretical analysis, the NPs degradation kinetics on MoS_2 can be schematically illustrated in Figure 8. Overall, the NPs' stability is affected by surface reaction with ambient atmosphere and interaction with the support.[23] Under vacuum or N_2 environments, the NP-support interaction is a critical factor that controls sintering behaviors. In this case, the Au@Pt NPs display less stability compared to Pt NPs on MoS_2, due to less Pt in contact with MoS_2. For Pt NPs on MoS_2 in H_2 (Figure 8a,b), hydrogen adsorption weakens NPs adhesion with MoS_2 at rt and elevated temperatures, resulting in more diffusion and migration of NPs on the support. In contrast, Au@Pt NPs in H_2 display better sintering resistance compared to Pt in a H_2 environment. This can be explained by H_2 induced size-dependent structural change in Au@Pt NPs (Figure 8c,d). As temperature rises, small NPs are easier to transform into alloy than large NPs due to H_2 dissociation, resulting in a decrease of surface Pt atoms and an increase of Pt in contact with MoS_2 support. Therefore, such H_2 promoted alloying kinetics enhances the stability of small size Au@Pt NPs due to two reasons: (1) the decrease of surface Pt mitigates the metal−H interactions and thus reduces the hydrogen adsorption induced weakening of adhesion with MoS_2, and (2) the increase of Pt in contact with MoS_2 strengthens the anchoring of NPs on MoS_2 support. Experimentally, this is seen as relatively stable

https://dx.doi.org/10.1021/acsnano.9b08757
ACS Nano 2020, 14, 4074−4086

small Au@Pt but rotation and diffusion of similar size Pt NPs under H_2 gas. Furthermore, it is worth mentioning that the physical properties of support materials, such as surface morphology, can also influence the degradation mechanism. This can be seen from the sintering behaviors of commercial Pt/C under H_2 gas as shown in Figure S15. The circles highlighted regions that Pt NPs undergo very complex dynamics involving PMC and possibly Ostwald ripening due to both movement and diminish of small NPs. In addition, morphology change of carbon indicates the support is not stable at elevated temperature under H_2 and thus will have extra impact on sintering mechanisms. It has been reported that porous carbon support such as high surface area carbon can constrain the NPs and enhance the sintering resistance compared to solid carbon such as Vulcan.[25] Correspondingly, a flat support allows more free movements of NPs and thus tends to enhance the mobility. Under our conditions, MoS_2 provides a smoother 2D surface than carbon support so the NPs rotation and migration can be easier when particle-support adhesion is weak for the case of Pt in H_2 and thus allow further oriented attachment for particle coalescence (Figure 4b). As such, Pt and Au@Pt NPs sintering behavior on MoS_2 can be more possibly guided by PMC.

CONCLUSION

The present work provides study of catalysts sintering dynamics of Pt and Au@Pt on MoS_2 nanoflakes under vacuum and various gases environment including N_2, H_2, and air by *in situ* gas-cell TEM approach. It is found that the type of environment, size of NPs, and composition modification (core−shell design) are important factors in controlling the degradation mechanism over MoS_2 substrates. The observations are summarized as **Effect of environment:** while it was found that PMC was the main mechanism that led to Pt and Au@Pt NPs degradation under vacuum, N_2, and H_2 environments, the degradation of MoS_2 substrate was prominent under exposure to air at high temperatures. In addition, the Pt NPs were less stable under H_2 environment when compared with the Pt NPs under vacuum or N_2. This was explained by Pt−H interactions that weaken the adhesion of Pt with MoS_2. **Effect of NP composition:** under H_2, the stability of Au@Pt NPs was higher in comparison to Pt NPs. This phenomenon was attributed to H_2 interactions with metals by promoting the alloying of Pt−Au thus reducing the number of Pt at the surface (reducing H_2 dissociation) and increasing Pt atoms in contact with MoS_2. **Effect of particle size:** The alloying effect promoted by H_2 was more pronounced in small size Au@Pt NPs resulting in higher sintering resistance in comparison to large size Au@Pt NPs and similar size Pt NPs. Therefore, how Au@Pt core−shell structure influence the thermal degradation of NPs in atmospheric gas environment are demonstrated. These findings suggest that although H_2 decreases sintering resistant of Pt NPs on MoS_2, the core−shell NPs can be stabilized by carefully designing their structure and composition taking advantage of metal−gas interactions. In addition, insights on how 2D supports influence degradation behaviors of pristine and bimetallic core−shell NPs could benefit the future design of substrate-supported catalyst with better sintering resistance. We believe the presented *in situ* study is crucial for understanding catalyst behaviors at conditions that are closer to real applications such as at elevated temperatures and with exposure to various atmospheric gases.

METHODS

Chemicals. MoS_2 powder (<2 μm, 99%, Sigma-Aldrich), gold chloride $AuCl_3$ (>99.99%, Sigma-Aldrich), and potassium tetrachloroplatinate K_2PtCl_4 (>99.9%, Sigma-Aldrich) were used as received.

MoS_2 Synthesis and Exfoliation. Bulk MoS_2 powder was mixed with isopropyl alcohol (IPA) at a concentration of 20 mg/mL. The mixture was first sonicated for 5 h in a bath sonicator (Branson 3800, 40 kHz, 110 W) and then centrifuged at 2000 rpm for 30 min (Thermo Scientific, Legend Micro 21). The obtained supernatant was collected and centrifuged at 1500 rpm for 15 min. After that, the sediment was taken out, washed twice with DI water, and redispersed in fresh DI water before further characterization.

Deposition of Pt and Au@Pt Core−Shell NPs on MoS_2. Synthesis of Pt NPs on MoS_2 is based on the method reported elsewhere.[70] In brief, 20 mM K_2PtCl_4 was added into MoS_2 dispersion, followed by a 10 min UV irritation under an UV lamp (Blak-Ray B-100AP) at full intensity. The obtained MoS_2 with Pt was then sonicated for 5 min, centrifuged at 5000 rpm for 10 min, and washed with DI water three times before characterization.

Au@Pt core−shell NPs on MoS_2 is based on a two-step seed growth method. Ten microliters of 20 mM $AuCl_3$ aqueous solution was added into exfoliated MoS_2 dispersion with mild shaking. A galvanic displacement reaction occurs, resulting in the spontaneous reduction of Au ions to Au seed deposited on MoS_2.[71] The obtained solution containing MoS_2 with Au seeds was centrifuged and washed with DI water two times before redispersion in 4 mL of DI water. K_2PtCl_4 (20 mM) with a 1:1 molar ratio of $AuCl_3$ was then added, followed by UV irradiation for 10 min at full intensity. After 5 min sonication, the resulting solution was centrifuged and washed with DI water three times before any further characterization. Although these methods are ligand-free processes, it is worth mentioning that synthesis conditions may result in different NPs stability; therefore, systemic studies are helpful to further elaborate this.

***In Situ* Gas Flow TEM Experiment.** A gas-cell TEM holder with pair of silicon microchips (Hummingbird Scientific) was used (Figure 2a−c). Each of the microchips has an electron transparent silicon nitride (Si_3N_4) viewing window with 50 nm in thickness and 200 × 50 μm^2 in dimension. Spacers with 250 nm thickness on one microchip are used to control the top and bottom distance in gas reactor. One droplet containing 1 μL of liquid sample dispersion was added on one of the microchips with a heater and dried under air. The viewing windows were aligned in parallel to provide a maximized viewing area. For *in situ* heating in vacuum without any gas, the window on small microchip was removed to leave a hole and then paired with large microchip with sample on that. The gas channels on the *in situ* gas holder were blocked to allow the sample stay in vacuum condition. For *in situ* heating in gas environments, 100% pure N_2, H_2, and air (containing ∼21 vol % O_2) flow was introduced through gas channels with constant volumetric flow rate of 0.5 sccm. The pressure inside the cell is approximately 1 atm. Local temperature at the sample area is controlled and monitored in real-time. Figure 2d shows the temperature profile for each *in situ* experiment. After loading the holder and flowing gas at rt for 30 min, the temperature was first ramped to 100 °C, followed by a 25 °C increase every 5 min. After reaching 400 °C for 5 min the temperature was ramped down back to rt. Images were taken at rt, 100, 150, 200, 250, 300, 350, 400 °C and back to rt, as indicated by red dots in Figure 2d. The electron beam was kept blocked except during initial TEM alignment, focusing and image acquisition. Acquisition time for each image was kept within 3s for each imaging period to minimize electron beam effects. All *in situ* experimental parameters were kept consistent except the sample ambience and were carried out using a field emission JEOL 2100F microscope operated at 200 kV. Filtered HRTEM images were obtained by applying band-pass filter in DigitalMicrograph software.

Electron Microscopy Characterization. The morphology of *in situ* microchips were characterized by a variable-pressure SEM Hitachi S-3000N operated at 5 kV. For STEM and EELS characterization, deposited Pt and Au@Pt core−shell NPs on MoS_2 were drop casted on a lacy copper grid. *Post situ* sample on microchips were

https://dx.doi.org/10.1021/acsnano.9b08757
ACS Nano 2020, 14, 4074−4086

characterized using a self-designed (S)TEM specimen holder (patent pending). STEM images were acquired by a spherical aberration corrected JEOL JEM-ARM 200CF with a cold field emission source operating at 200 kV, at 22 mrad convergence semiangle. False-color STEM images were obtained by ImageJ.[72] Energy dispersive spectrometer (EDS) spectra were acquired with a Oxford X-Max 100TLE windowless silicon drift detector. TrueMap was used for all EDS signal collection to correct the overlapping of Mo, S, Au, and Pt signals. Electron energy loss spectra were acquired using a Gatan GIF Quantum spectrometer with an entrance aperture of 5 mm in dual-EELS mode. EELS maps were extracted from Mo $L_{2,3}$ edges, S K edge, Au, and Pt $M_{4,5}$ edges using power law fitting background subtraction after energy drift correction and Fourier-ratio deconvolution.

Density Functional Theory Calculations. The DFT calculations are performed using the Vienna *ab initio* simulation package[73−76] with the Perdew−Burke−Ernzerhof (PBE)[77] and projector-augmented wave potentials using a cutoff energy of 400 eV. Dispersion interactions are included using DFT-D2.[78] We also compared the results using Tkatchenko−Scheffler (TS) dispersion.[79,80] The calculations are carried out using a 7 × 7 surface supercell for MoS_2 where the Brillouin zone is sampled at the γ point. The structural optimization is terminated when all force components are less than 0.01 eV/Å. The MoS_2/Pt_{20} structure was obtained from our previous study.[70]

ASSOCIATED CONTENT

Supporting Information

The Supporting Information is available free of charge at https://pubs.acs.org/doi/10.1021/acsnano.9b08757.

EDS profiles of Pt and Au@Pt, EELS mappings of Au@Pt, SAED patterns, Au@Pt NPs annealing in air, HRTEM images of Pt and Au@Pt annealing in vacuum and N_2, enlarged HRTEM in Figure 5a, EELS mappings of Au@Pt NPs after annealing in vacuum and H_2, computational details, temperature effects on stability, and TEM images of Pt/C annealing in H_2 (PDF)

AUTHOR INFORMATION

Corresponding Authors

Wissam A. Saidi − *Department of Mechanical Engineering and Materials Science, University of Pittsburgh, Pittsburgh, Pennsylvania 15261, United States;* orcid.org/0000-0001-6714-4832; Email: alsaidi@pitt.edu

Yuzi Liu − *Center for Nanoscale Materials, Argonne National Laboratory, Argonne, Illinois 60439, United States;* orcid.org/0000-0002-8733-1683; Email: yuziliu@anl.gov

Reza Shahbazian-Yassar − *Department of Mechanical and Industrial Engineering, University of Illinois at Chicago, Chicago, Illinois 60607, United States;* orcid.org/0000-0002-7744-4780; Email: rsyassar@uic.edu

Authors

Boao Song − *Department of Mechanical and Industrial Engineering, University of Illinois at Chicago, Chicago, Illinois 60607, United States;* orcid.org/0000-0003-3124-3235

Timothy T. Yang − *Department of Mechanical Engineering and Materials Science, University of Pittsburgh, Pittsburgh, Pennsylvania 15261, United States;* orcid.org/0000-0002-5785-0511

Yifei Yuan − *Department of Mechanical and Industrial Engineering, University of Illinois at Chicago, Chicago, Illinois 60607, United States;* orcid.org/0000-0002-2360-8794

Soroosh Sharifi-Asl − *Department of Mechanical and Industrial Engineering, University of Illinois at Chicago, Chicago, Illinois 60607, United States;* orcid.org/0000-0003-0441-9231

Meng Cheng − *Department of Mechanical and Industrial Engineering, University of Illinois at Chicago, Chicago, Illinois 60607, United States*

Complete contact information is available at: https://pubs.acs.org/10.1021/acsnano.9b08757

Author Contributions

B.S. and R.S.-Y. conceived the idea. B.S. carried out the (S)TEM and *in situ* TEM experiments. T.Y. and W.S. carried out the DFT calculations. Y.L., Y.Y., S.S.-A., and M.C. provided necessary (S)TEM and SEM support. B.S. wrote the paper under the direction of R.S.-Y. All authors contributed to the discussion and writing of the manuscript.

Notes

The authors declare no competing financial interest.

ACKNOWLEDGMENTS

R.S.-Y. acknowledges financial support from the National Science Foundation (Award No. DMR-1809439). W.S. acknowledges financial support from the National Science Foundation (Award No. DMR-1809085). The computational work is supported in part by the University of Pittsburgh Center for Research Computing through the resources provided. This work was performed, in part, at the Center for Nanoscale Materials, a U.S. Department of Energy Office of Science User Facility, and supported by the U.S. Department of Energy, Office of Science, under Contract No. DE-AC02-06CH11357. This work made use of the JEOL JEM-ARM 200CF and JEOL JEM-3010 in the Electron Microscopy Service (Research Resources Center, UIC). The acquisition of the UIC JEOL JEM-ARM 200CF was supported by a MRI-R2 grant from the National Science Foundation (DMR-0959470). We thank Dr. Fengyuan Shi from UIC for the assistance on (S)TEM experiments.

REFERENCES

(1) Julkapli, N. M.; Bagheri, S. Graphene Supported Heterogeneous Catalysts: An Overview. *Int. J. Hydrogen Energy* **2015**, *40*, 948−979.

(2) Yin, Z.; Chen, B.; Bosman, M.; Cao, X.; Chen, J.; Zheng, B.; Zhang, H. Au Nanoparticle-Modified MoS_2 Nanosheet-Based Photoelectrochemical Cells for Water Splitting. *Small* **2014**, *10*, 3537−3543.

(3) Zeng, Z.; Tan, C.; Huang, X.; Bao, S.; Zhang, H. Growth of Noble Metal Nanoparticles on Single-Layer TiS_2 and TaS_2 Nanosheets for Hydrogen Evolution Reaction. *Energy Environ. Sci.* **2014**, *7*, 797−803.

(4) Wang, Y.; Zhang, X.; Luo, Z.; Huang, X.; Tan, C.; Li, H.; Zheng, B.; Li, B.; Huang, Y.; Yang, J.; Zong, Y.; Ying, Y.; Zhang, H. Liquid-Phase Growth of Platinum Nanoparticles on Molybdenum Trioxide Nanosheets: An Enhanced Catalyst with Intrinsic Peroxidase-Like Catalytic Activity. *Nanoscale* **2014**, *6*, 12340−12344.

(5) Deng, D.; Novoselov, K. S.; Fu, Q.; Zheng, N.; Tian, Z.; Bao, X. Catalysis with Two-Dimensional Materials and Their Heterostructures. *Nat. Nanotechnol.* **2016**, *11*, 218.

(6) Cai, Q.; Mateti, S.; Watanabe, K.; Taniguchi, T.; Huang, S.; Chen, Y.; Li, L. H. Boron Nitride Nanosheet-Veiled Gold Nanoparticles for Surface-Enhanced Raman Scattering. *ACS Appl. Mater. Interfaces* **2016**, *8*, 15630−15636.

(7) Sun, H.; Chao, J.; Zuo, X.; Su, S.; Liu, X.; Yuwen, L.; Fan, C.; Wang, L. Gold Nanoparticle-Decorated MoS_2 Nanosheets for Simultaneous Detection of Ascorbic Acid, Dopamine and Uric Acid. *RSC Adv.* **2014**, *4*, 27625−27629.

(8) Jasuja, K.; Berry, V. Implantation and Growth of Dendritic Gold Nanostructures on Graphene Derivatives: Electrical Property Tailoring and Raman Enhancement. *ACS Nano* **2009**, *3*, 2358−2366.

(9) Lu, J.; Lu, J. H.; Liu, H.; Liu, B.; Gong, L.; Tok, E. S.; Loh, K. P.; Sow, C. H. Microlandscaping of Au Nanoparticles on Few-Layer MoS_2 Films for Chemical Sensing. *Small* **2015**, *11*, 1792−1800.
(10) Yang, X.; Liu, W.; Xiong, M.; Zhang, Y.; Liang, T.; Yang, J.; Xu, M.; Ye, J.; Chen, H. Au Nanoparticles on Ultrathin MoS_2 Sheets for Plasmonic Organic Solar Cells. *J. Mater. Chem. A* **2014**, *2*, 14798−14806.
(11) Yue, W.; Yang, S.; Ren, Y.; Yang, X. *In Situ* Growth of Sn, SnO on Graphene Nanosheets and Their Application as Anode Materials for Lithium-Ion Batteries. *Electrochim. Acta* **2013**, *92*, 412−420.
(12) Asadi, M.; Kumar, B.; Liu, C.; Phillips, P.; Yasaei, P.; Behranginia, A.; Zapol, P.; Klie, R. F.; Curtiss, L. A.; Salehi-Khojin, A. Cathode Based on Molybdenum Disulfide Nanoflakes for Lithium-Oxygen Batteries. *ACS Nano* **2016**, *10*, 2167−2175.
(13) Huang, X.; Zeng, Z.; Bao, S.; Wang, M.; Qi, X.; Fan, Z.; Zhang, H. Solution-Phase Epitaxial Growth of Noble Metal Nanostructures on Dispersible Single-Layer Molybdenum Disulfide Nanosheets. *Nat. Commun.* **2013**, *4*, 1−8.
(14) Hou, D.; Zhou, W.; Liu, X.; Zhou, K.; Xie, J.; Li, G.; Chen, S. Pt Nanoparticles/MoS_2 Nanosheets/Carbon Fibers as Efficient Catalyst for the Hydrogen Evolution Reaction. *Electrochim. Acta* **2015**, *166*, 26−31.
(15) Yang, T. T.; Tan, T. L.; Saidi, W. A. High Activity toward the Hydrogen Evolution Reaction on the Edges of MoS_2-Supported Platinum Nanoclusters Using Cluster Expansion and Electrochemical Modeling. *Chem. Mater.* **2020**, *32*, 1315−1321.
(16) Cheng, Y.; Lu, S.; Liao, F.; Liu, L.; Li, Y.; Shao, M. Rh-MoS_2 Nanocomposite Catalysts with Pt-Like Activity for Hydrogen Evolution Reaction. *Adv. Funct. Mater.* **2017**, *27*, 1700359.
(17) Bose, R.; Jin, Z.; Shin, S.; Kim, S.; Lee, S.; Min, Y.-S. Co-Catalytic Effects of CoS_2 on the Activity of the MoS_2 Catalyst for Electrochemical Hydrogen Evolution. *Langmuir* **2017**, *33*, 5628−5635.
(18) Kim, M.; Anjum, M. A. R.; Lee, M.; Lee, B. J.; Lee, J. S. Activating MoS_2 Basal Plane with Ni_2P Nanoparticles for Pt-Like Hydrogen Evolution Reaction in Acidic Media. *Adv. Funct. Mater.* **2019**, *29*, 1809151.
(19) Argyle, M.; Bartholomew, C. Heterogeneous Catalyst Deactivation and Regeneration: A Review. *Catalysts* **2015**, *5*, 145−269.
(20) Dai, S.; Chou, J. P.; Wang, K. W.; Hsu, Y. Y.; Hu, A.; Pan, X.; Chen, T. Y. Platinum-Trimer Decorated Cobalt-Palladium Core-Shell Nanocatalyst with Promising Performance for Oxygen Reduction Reaction. *Nat. Commun.* **2019**, *10*, 1−10.
(21) Zhao, Y.; Yang, K. R.; Wang, Z.; Yan, X.; Cao, S.; Ye, Y.; Dong, Q.; Zhang, X.; Thorne, J. E.; Jin, L.; Materna, K. L.; Trimpalis, A.; Bai, H.; Fakra, S. C.; Zhong, X.; Wang, P.; Pan, X.; Guo, J.; Flytzani-Stephanopoulos, M.; Brudvig, G. W.; et al. Stable Iridium Dinuclear Heterogeneous Catalysts Supported on Metal-Oxide Substrate for Solar Water Oxidation. *Proc. Natl. Acad. Sci. U. S. A.* **2018**, *115*, 2902−2907.
(22) Bian, T.; Zhang, H.; Jiang, Y.; Jin, C.; Wu, J.; Yang, H.; Yang, D. Epitaxial Growth of Twinned Au-Pt Core-Shell Star-Shaped Decahedra as Highly Durable Electrocatalysts. *Nano Lett.* **2015**, *15*, 7808−7815.
(23) Campbell, C. T.; Sellers, J. R. V. Anchored Metal Nanoparticles: Effects of Support and Size on Their Energy, Sintering Resistance and Reactivity. *Faraday Discuss.* **2013**, *162*, 9−30.
(24) Li, W. Z.; Kovarik, L.; Mei, D.; Liu, J.; Wang, Y.; Peden, C. H. Stable Platinum Nanoparticles on Specific $MgAl_2O_4$ Spinel Facets at High Temperatures in Oxidizing Atmospheres. *Nat. Commun.* **2013**, *4*, 1−8.
(25) Padgett, E.; Yarlagadda, V.; Holtz, M. E.; Ko, M.; Levin, B. D. A.; Kukreja, R. S.; Ziegelbauer, J. M.; Andrews, R. N.; Ilavsky, J.; Kongkanand, A.; Muller, D. A. Mitigation of PEM Fuel Cell Catalyst Degradation with Porous Carbon Supports. *J. Electrochem. Soc.* **2019**, *166*, F198−F207.
(26) Jin, Z.; Nackashi, D.; Lu, W.; Kittrell, C.; Tour, J. M. Decoration, Migration, and Aggregation of Palladium Nanoparticles on Graphene Sheets. *Chem. Mater.* **2010**, *22*, 5695−5699.
(27) Su, S.; Zhang, C.; Yuwen, L.; Liu, X.; Wang, L.; Fan, C.; Wang, L. Uniform Au@Pt Core-Shell Nanodendrites Supported on Molybdenum Disulfide Nanosheets for the Methanol Oxidation Reaction. *Nanoscale* **2016**, *8*, 602−608.
(28) Gilbert, J. A.; Kariuki, N. N.; Wang, X.; Kropf, A. J.; Yu, K.; Groom, D. J.; Ferreira, P. J.; Morgan, D.; Myers, D. J. Pt Catalyst Degradation in Aqueous and Fuel Cell Environments Studied *via* In-Operando Anomalous Small-Angle X-Ray Scattering. *Electrochim. Acta* **2015**, *173*, 223−234.
(29) Matos, J.; Ono, L. K.; Behafarid, F.; Croy, J. R.; Mostafa, S.; DeLaRiva, A. T.; Datye, A. K.; Frenkel, A. I.; Roldan Cuenya, B. *In Situ* Coarsening Study of Inverse Micelle-Prepared Pt Nanoparticles Supported on Gamma-Al_2O_3: Pretreatment and Environmental Effects. *Phys. Chem. Chem. Phys.* **2012**, *14*, 11457−11467.
(30) Wang, L.; Zhang, W.; Wang, S.; Gao, Z.; Luo, Z.; Wang, X.; Zeng, R.; Li, A.; Li, H.; Wang, M.; Zheng, X.; Zhu, J.; Zhang, W.; Ma, C.; Si, R.; Zeng, J. Atomic-Level Insights in Optimizing Reaction Paths for Hydroformylation Reaction over Rh/CoO Single-Atom Catalyst. *Nat. Commun.* **2016**, *7*, 1−8.
(31) Bonifacio, C. S.; Carenco, S.; Wu, C. H.; House, S. D.; Bluhm, H.; Yang, J. C. Thermal Stability of Core-Shell Nanoparticles: A Combined *In Situ* Study by XPS and TEM. *Chem. Mater.* **2015**, *27*, 6960−6968.
(32) Chi, M.; Wang, C.; Lei, Y.; Wang, G.; Li, D.; More, K. L.; Lupini, A.; Allard, L. F.; Markovic, N. M.; Stamenkovic, V. R. Surface Faceting and Elemental Diffusion Behaviour at Atomic Scale for Alloy Nanoparticles During *In Situ* Annealing. *Nat. Commun.* **2015**, *6*, 8925.
(33) Cichocka, M. O.; Zhao, J.; Bachmatiuk, A.; Quang, H. T.; Gorantla, S. M.; Gonzalez-Martinez, I. G.; Fu, L.; Eckert, J.; Warner, J. H.; Rümmeli, M. H. *In Situ* Observations of Pt Nanoparticles Coalescing inside Carbon Nanotubes. *RSC Adv.* **2014**, *4*, 49442−49445.
(34) Yuk, J. M.; Jeong, M.; Kim, S. Y.; Seo, H. K.; Kim, J.; Lee, J. Y. *In Situ* Atomic Imaging of Coalescence of Au Nanoparticles on Graphene: Rotation and Grain Boundary Migration. *Chem. Commun. (Cambridge, U. K.)* **2013**, *49*, 11479−11481.
(35) Liu, Y.; Sun, Y. Electron Beam Induced Evolution in Au, Ag, and Interfaced Heterogeneous Au/Ag Nanoparticles. *Nanoscale* **2015**, *7*, 13687−13693.
(36) Li, Y.; Zakharov, D.; Zhao, S.; Tappero, R.; Jung, U.; Elsen, A.; Baumann, P.; Nuzzo, R. G.; Stach, E. A.; Frenkel, A. I. Complex Structural Dynamics of Nanocatalysts Revealed in Operando Conditions by Correlated Imaging and Spectroscopy Probes. *Nat. Commun.* **2015**, *6*, 7583.
(37) Chen, H.; Yu, Y.; Xin, H. L.; Newton, K. A.; Holtz, M. E.; Wang, D.; Muller, D. A.; Abruña, H. D.; DiSalvo, F. J. Coalescence in the Thermal Annealing of Nanoparticles: An *In Situ* STEM Study of the Growth Mechanisms of Ordered Pt-Fe Nanoparticles in a KCl Matrix. *Chem. Mater.* **2013**, *25*, 1436−1442.
(38) Li, J.; Wang, Z.; Chen, C.; Huang, S. Atomic-Scale Observation of Migration and Coalescence of Au Nanoclusters on YSZ Surface by Aberration-Corrected STEM. *Sci. Rep.* **2015**, *4*, 5521.
(39) Gao, W.; Tieu, P.; Addiego, C.; Ma, Y.; Wu, J.; Pan, X. Probing the Dynamics of Nanoparticle Formation from a Precursor at Atomic Resolution. *Sci. Adv.* **2019**, *5*, No. eaau9590.
(40) Taheri, M. L.; Stach, E. A.; Arslan, I.; Crozier, P. A.; Kabius, B. C.; LaGrange, T.; Minor, A. M.; Takeda, S.; Tanase, M.; Wagner, J. B. Current Status and Future Directions for *In Situ* Transmission Electron Microscopy. *Ultramicroscopy* **2016**, *170*, 86−95.
(41) Vara, M.; Roling, L. T.; Wang, X.; Elnabawy, A. O.; Hood, Z. D.; Chi, M.; Mavrikakis, M.; Xia, Y. Understanding the Thermal Stability of Palladium-Platinum Core-Shell Nanocrystals by *In Situ* Transmission Electron Microscopy and Density Functional Theory. *ACS Nano* **2017**, *11*, 4571−4581.
(42) Chen, Q.; He, K.; Robertson, A. W.; Kirkland, A. I.; Warner, J. H. Atomic Structure and Dynamics of Epitaxial 2D Crystalline Gold

https://dx.doi.org/10.1021/acsnano.9b08757
ACS Nano 2020, 14, 4074−4086

on Graphene at Elevated Temperatures. *ACS Nano* **2016**, *10*, 10418−10427.
(43) Simonsen, S. B.; Chorkendorff, I.; Dahl, S.; Skoglundh, M.; Sehested, J.; Helveg, S. Ostwald Ripening in a Pt/SiO_2 Model Catalyst Studied by *In Situ* TEM. *J. Catal.* **2011**, *281*, 147−155.
(44) Simonsen, S. B.; Chorkendorff, I.; Dahl, S.; Skoglundh, M.; Sehested, J.; Helveg, S. Direct Observations of Oxygen-Induced Platinum Nanoparticle Pipening Studied by *In Situ* TEM. *J. Am. Chem. Soc.* **2010**, *132*, 7968−7975.
(45) Simonsen, S. B.; Wang, Y.; Jensen, J. O.; Zhang, W. Coarsening of Carbon Black Supported Pt Nanoparticles in Hydrogen. *Nanotechnology* **2017**, *28*, 475710.
(46) Lawrence, E. L.; Crozier, P. A. Oxygen Transfer at Metal-Reducible Oxide Nanocatalyst Interfaces: Contrasting Carbon Growth from Ethane and Ethylene. *ACS Appl. Nano Mater.* **2018**, *1*, 1360−1369.
(47) Lin, P. A.; Gomez-Ballesteros, J. L.; Burgos, J. C.; Balbuena, P. B.; Natarajan, B.; Sharma, R. Direct Evidence of Atomic-Scale Structural Fluctuations in Catalyst Nanoparticles. *J. Catal.* **2017**, *349*, 149−155.
(48) Zhu, Y.; Sushko, P. V.; Melzer, D.; Jensen, E.; Kovarik, L.; Ophus, C.; Sanchez-Sanchez, M.; Lercher, J. A.; Browning, N. D. Formation of Oxygen Radical Sites on Movnbteox by Cooperative Electron Redistribution. *J. Am. Chem. Soc.* **2017**, *139*, 12342−12345.
(49) Wang, C.-M.; Genc, A.; Cheng, H.; Pullan, L.; Baer, D. R.; Bruemmer, S. M. *In Situ* TEM Visualization of Vacancy Injection and Chemical Partition During Oxidation of Ni-Cr Nanoparticles. *Sci. Rep.* **2015**, *4*, 3683.
(50) Wu, Y. A.; Li, L.; Li, Z.; Kinaci, A.; Chan, M. K.; Sun, Y.; Guest, J. R.; McNulty, I.; Rajh, T.; Liu, Y. Visualizing Redox Dynamics of a Single Ag/AgCl Heterogeneous Nanocatalyst at Atomic Resolution. *ACS Nano* **2016**, *10*, 3738−3746.
(51) Xin, H. L.; Niu, K.; Alsem, D. H.; Zheng, H. *In Situ* TEM Study of Catalytic Nanoparticle Reactions in Atmospheric Pressure Gas Environment. *Microsc. Microanal.* **2013**, *19*, 1558−1568.
(52) Dai, S.; Hou, Y.; Onoue, M.; Zhang, S.; Gao, W.; Yan, X.; Graham, G. W.; Wu, R.; Pan, X. Revealing Surface Elemental Composition and Dynamic Processes Involved in Facet-Dependent Oxidation of Pt_3Co Nanoparticles *via In Situ* Transmission Electron Microscopy. *Nano Lett.* **2017**, *17*, 4683−4688.
(53) Matsubu, J. C.; Zhang, S.; DeRita, L.; Marinkovic, N. S.; Chen, J. G.; Graham, G. W.; Pan, X.; Christopher, P. Adsorbate-Mediated Strong Metal-Support Interactions in Oxide-Supported Rh Catalysts. *Nat. Chem.* **2017**, *9*, 120−127.
(54) Prestat, E.; Kulzick, M. A.; Dietrich, P. J.; Smith, M. M.; Tien, M. E. P.; Burke, M. G.; Haigh, S. J.; Zaluzec, N. J. *In Situ* Industrial Bimetallic Catalyst Characterization Using Scanning Transmission Electron Microscopy and X-Ray Absorption Spectroscopy at One Atmosphere and Elevated Temperature. *ChemPhysChem* **2017**, *18*, 2151−2156.
(55) Dembélé, K.; Bahri, M.; Melinte, G.; Hirlimann, C.; Berliet, A.; Maury, S.; Gay, A. S.; Ersen, O. Insight by *In Situ* Gas Electron Microscopy on the Thermal Behaviour and Surface Reactivity of Cobalt Nanoparticles. *ChemCatChem* **2018**, *10*, 4004−4009.
(56) Zhang, X.; Meng, J.; Zhu, B.; Yu, J.; Zou, S.; Zhang, Z.; Gao, Y.; Wang, Y. *In Situ* TEM Studies of the Shape Evolution of Pd Nanocrystals under Oxygen and Hydrogen Environments at Atmospheric Pressure. *Chem. Commun. (Cambridge, U. K.)* **2017**, *53*, 13213−13216.
(57) Altantzis, T.; Lobato, I.; De Backer, A.; Béché, A.; Zhang, Y.; Basak, S.; Porcu, M.; Xu, Q.; Sánchez-Iglesias, A.; Liz-Marzán, L. M.; Van Tendeloo, G.; Van Aert, S.; Bals, S. Three-Dimensional Quantification of the Facet Evolution of Pt Nanoparticles in a Variable Gaseous Environment. *Nano Lett.* **2019**, *19*, 477−481.
(58) Stach, E. A.; Li, Y.; Zhao, S.; Gamalski, A.; Zakharov, D.; Tappero, R.; Chen-Weigart, K.; Thieme, J.; Jung, U.; Elsen, A.; Wu, Q.; Orlov, A.; Chen, J.; Nuzzo, R. G.; Frenkel, A. Characterizing Working Catalysts with Correlated Electron and Photon Probes. *Microsc. Microanal.* **2015**, *21*, 563−564.
(59) Avanesian, T.; Dai, S.; Kale, M. J.; Graham, G. W.; Pan, X.; Christopher, P. Quantitative and Atomic-Scale View of Co-Induced Pt Nanoparticle Surface Reconstruction at Saturation Coverage *via* DFT Calculations Coupled with *In Situ* TEM and IR. *J. Am. Chem. Soc.* **2017**, *139*, 4551−4558.
(60) Jiang, Y.; Li, H.; Wu, Z.; Ye, W.; Zhang, H.; Wang, Y.; Sun, C.; Zhang, Z. *In Situ* Observation of Hydrogen-Induced Surface Faceting for Palladium-Copper Nanocrystals at Atmospheric Pressure. *Angew. Chem., Int. Ed.* **2016**, *55*, 12427−12430.
(61) Tan, S. F.; Chee, S. W.; Baraissov, Z.; Jin, H.; Tan, T. L.; Mirsaidov, U. Real-Time Imaging of Nanoscale Redox Reactions over Bimetallic Nanoparticles. *Adv. Funct. Mater.* **2019**, *29*, 1903242.
(62) Sapountzi, F. M.; Gracia, J. M.; Weststrate, C. J.; Fredriksson, H. O. A.; Niemantsverdriet, J. W. Electrocatalysts for the Generation of Hydrogen, Oxygen and Synthesis Gas. *Prog. Energy Combust. Sci.* **2017**, *58*, 1−35.
(63) Hansen, T. W.; DeLaRiva, A. T.; Challa, S. R.; Datye, A. K. Sintering of Catalytic Nanoparticles: Particle Migration or Ostwald Ripening? *Acc. Chem. Res.* **2013**, *46*, 1720−1730.
(64) Granqvist, C. G.; Buhrman, R. A. Size Distributions for Supported Metal Catalysts: Coalescence Growth *versus* Ostwald Ripening. *J. Catal.* **1976**, *42*, 477−479.
(65) Ye, G.; Gong, Y.; Lin, J.; Li, B.; He, Y.; Pantelides, S. T.; Zhou, W.; Vajtai, R.; Ajayan, P. M. Defects Engineered Monolayer MoS_2 for Improved Hydrogen Evolution Reaction. *Nano Lett.* **2016**, *16*, 1097−1103.
(66) Nørskov, J. K.; Bligaard, T.; Logadottir, A.; Kitchin, J. R.; Chen, J. G.; Pandelov, S.; Stimming, U. Trends in the Exchange Current for Hydrogen Evolution. *J. Electrochem. Soc.* **2005**, *152*, J23−J26.
(67) Saidi, W. A. Trends in the Adsorption and Growth Morphology of Metals on the $MoS_2(001)$ Surface. *Cryst. Growth Des.* **2015**, *15*, 3190−3200.
(68) Saidi, W. A. Density Functional Theory Study of Nucleation and Growth of Pt Nanoparticles on $MoS_2(001)$ Surface. *Cryst. Growth Des.* **2015**, *15*, 642−652.
(69) Yang, T. T.; Saidi, W. A. Tuning the Hydrogen Evolution Activity of β-Mo_2C Nanoparticles *via* Control of Their Growth Conditions. *Nanoscale* **2017**, *9*, 3252−3260.
(70) Shi, Y.; Song, B.; Shahbazian-Yassar, R.; Zhao, J.; Saidi, W. A. Experimentally Validated Structures of Supported Metal Nanoclusters on MoS_2. *J. Phys. Chem. Lett.* **2018**, *9*, 2972−2978.
(71) Song, B.; He, K.; Yuan, Y.; Sharifi-Asl, S.; Cheng, M.; Lu, J.; Saidi, W. A.; Shahbazian-Yassar, R. *In Situ* Study of Nucleation and Growth Dynamics of Au Nanoparticles on MoS_2 Nanoflakes. *Nanoscale* **2018**, *10*, 15809−15818.
(72) Schneider, C. A.; Rasband, W. S.; Eliceiri, K. W. NIH Image to ImageJ: 25 Years of Image Analysis. *Nat. Methods* **2012**, *9*, 671−675.
(73) Kresse, G.; Furthmuller, J. Efficient Iterative Schemes for *Ab Initio* Total-Energy Calculations Using a Plane-Wave Basis Set. *Phys. Rev. B: Condens. Matter Mater. Phys.* **1996**, *54*, 11169−11186.
(74) Kresse, G.; Furthmüller, J. Efficiency of *Ab-Initio* Total Energy Calculations for Metals and Semiconductors Using a Plane-Wave Basis Set. *Comput. Mater. Sci.* **1996**, *6*, 15−50.
(75) Kresse, G.; Hafner, J. *Ab Initio* Molecular Dynamics for Liquid Metals. *Phys. Rev. B: Condens. Matter Mater. Phys.* **1993**, *47*, 558−561.
(76) Kresse, G.; Hafner, J. *Ab Initio* Molecular-Dynamics Simulation of the Liquid-Metal-Amorphous-Semiconductor Transition in Germanium. *Phys. Rev. B: Condens. Matter Mater. Phys.* **1994**, *49*, 14251−14269.
(77) Perdew, J. P.; Burke, K.; Ernzerhof, M. Generalized Gradient Approximation Made Simple. *Phys. Rev. Lett.* **1996**, *77*, 3865.
(78) Grimme, S. Accurate Description of van der Waals Complexes by Density Functional Theory Including Empirical Corrections. *J. Comput. Chem.* **2004**, *25*, 1463−1473.
(79) Tkatchenko, A.; Scheffler, M. Accurate Molecular van der Waals Interactions from Ground-State Electron Density and Free-Atom Reference Data. *Phys. Rev. Lett.* **2009**, *102*, 073005.

https://dx.doi.org/10.1021/acsnano.9b08757
ACS Nano 2020, 14, 4074−4086

(80) Al-Saidi, W.; Voora, V. K.; Jordan, K. D. An Assessment of the vdW-TS Method for Extended Systems. *J. Chem. Theory Comput.* **2012**, *8*, 1503−1513.

https://dx.doi.org/10.1021/acsnano.9b08757
ACS Nano 2020, 14, 4074−4086